Nuclear Materials and Energy 36 (2023) 101462

Contents lists available at ScienceDirect

Nuclear Materials and Energy

journal homepage: www.elsevier.com/locate/nme

Neutron Bragg edge tomography characterisation of residual strain in a laser-welded Eurofer97 joint

Bin Zhu [a], Nathanael Leung [a], Winfried Kockelmann [b], Michael Gorley [c], Mark J. Whiting [a], Yiqiang Wang [c,*], Tan Sui [a,d,*]

[a] School of Mechanical Engineering Sciences, University of Surrey, Guildford, Surrey GU2 7XH, UK
[b] Science and Technology Facilities Council (STFC), Rutherford Appleton Laboratory, ISIS Facility, Harwell OX11 0QX, UK
[c] United Kingdom Atomic Energy Authority, Culham Centre for Fusion Energy, Culham Science Centre, Abingdon, Oxon, OX14 3DB, UK
[d] National Physical Laboratory, Hampton Road, Teddington TW11 0LW, UK

ARTICLE INFO

Keywords:
Neutron Bragg edge imaging
Strain tomography
Laser-welded Eurofer97 joints

ABSTRACT

Nuclear fusion is a potential source of electricity which can address the environmental problems posed by fossil fuels. Eurofer97 steel is a primary structural material for breeding blanket and divertor components in fusion Tokamaks. Assembling and maintaining the structural integrity of these in-vessel components requires remote joint techniques, such as laser welding, although it induces immersive residual stress. The interaction of the residual strain and the heterogeneous microstructure degrades the mechanical performance of fusion components. However, an inspection of bulk residual strain distribution is still challenging. This study presents the residual strain distribution in the bulk of the weldment using volumetric tomographic reconstruction. A neutron Bragg edge imaging technique is used to obtain 2D angular projections. The 3D volumetric strain map is reconstructed from 2D residual strain projections using the filtered back projection technique. It is found that the laser welding technique generates a uniform residual strain field in the through-thickness direction. The results also demonstrate the potential of reconstructing volumetric residual strain distribution in bulk materials using fewer projections to reduce data redundancy and acquisition time for the neutron Bragg edge imaging technique.

1. Introduction

Nuclear fusion energy is a potential substitute source of electricity production, to solve dependence on fossil fuels, reduce carbon emissions and to provide a major contribution to net zero targets. Reduced-activation ferritic/martensitic (RAFM) steels, which are an evolution of high Cr Grade 91 steel, are widely used as structural materials in various in-vessel components for the DEMOnstration power plant (DEMO). Eurofer97, one of the RAFM steels, uses lower activation elements like tungsten, vanadium and tantalum in appropriate quantities. It is used as the European reference material for the EU-DEMO reactor because of its excellent mechanical properties: creep life, fracture, strength and ductility [1,2].

The in-vessel components in the fusion plant, such as pipes, breeding blanket and divertor cassette, have to utilise complex materials systems, complicated joining techniques and maintenance processes to enable their function under extreme operating conditions [3–5]. Laser welding is a promising technique that is used extensively in a wide range of industries to overcome intrinsic assembly and maintenance difficulties. Previous studies have demonstrated the feasibility of using remote laser tools to butt-weld in-vessel components [6,7]. However, the joining process induces substantial residual stress, and the laser-welded in-vessel components suffer from residual stress related issues, such as crack initiation and propagation, in extreme working conditions.

It is widely reported that residual stress aggravates cracking by enhancing the void formation rate and this can leads to premature failure [8,9]. Concerns about residual stress related cracking and other types of failure of welded joints have existed for conventional Grade 91 steel sheets and its derivatives, such as Eurofer97. Therefore, investigating the bulk distribution of residual stress inside the joint is critical to predicting crack initiation and maintaining structural integrity. To reduce the downtime arising from regular inspection frequency and to enable prediction of the longevity of engineering components, three-dimensional (3D) bulk investigation of residual strain distribution inside the material is necessary.

Non-destructive evaluation techniques are the key to achieving a

* Corresponding authors.
E-mail addresses: yiqiang.wang@ukaea.uk (Y. Wang), t.sui@surrey.ac.uk (T. Sui).

https://doi.org/10.1016/j.nme.2023.101462
Received 24 February 2023; Received in revised form 5 June 2023; Accepted 13 June 2023
Available online 15 June 2023

better understanding of internal structures, crack initiation and strain distribution of a weldment. Two-dimensional (2D) residual strain can be determined by synchrotron-based X-rays using spot-by-spot measurement [10–12]. The through-thickness residual strain is accessible using neutron diffraction, and the strain can be extended to 3D, owing to the high penetration of neutron particles. However, the millimetre-level resolution and long data acquisition time confine it to the investigation of subtle changes in the residual strain field in a large region. The high-resolution residual strain maps for a large region can be obtained using neutron Bragg edge imaging (NBEI), where the strain state is averaged over the beam path. Due to the residual strain distribution in the beam direction being neglected, investigating the complex residual strain fields varying through the sample thickness is still challenging.

Recently developed 3D tomographic reconstruction techniques can provide insight into the bulk of joints. Previous studies have demonstrated the feasibility of reconstructing strain fields under certain assumptions regarding the axisymmetric properties of lattice strains [13–18], enabling synchrotron-based X-ray diffraction techniques to reconstruct 3D residual strain in a limited region on the micro-scale [10,14,19,20]. Additionally, combining the tomographic reconstruction technique with NBEI allows the inspection of microstructures and strain fields for a large area simultaneously in a non-destructive way. This can reveal the heterogeneities undetected by conventional diffraction and imaging techniques. Most of these studies have investigated internal cracks and phase distribution through a 3D reconstructed model using NBEI [14,21,22]. Only a small number of studies report the tomographic strain reconstruction on a large scale, with appropriate assumptions. Efforts have been made to reconstruct residual strain for additively manufactured stainless steel by sequentially reconstructing a 3D model of lattice spacing, enabling the calculation of residual strain via a reference lattice spacing [23]. However, such a procedure is unsuitable for reconstructing weldments due to the difference in composition of different sub-regions of the weldment. To precisely describe the internal residual strain, the residual strain maps that present the collective strain distribution in sub-regions of weldment must be obtained before tomographic reconstruction can proceed. Furthermore, owing to the time-consuming nature of acquiring a large number of strain projections, it is desirable to reconstruct strain using a small number of projections, compared to conventional radiographic reconstruction, as the collection time of a Bragg edge projection is in the order or minutes or hours.

In this study, an attenuation and residual strain tomographic reconstruction was demonstrated on laser-welded Eurofer97. Reflected light microscopy was used to characterise the cross-section showing the dimension of the sub-regions of the weldment, and NBEI was used to obtain neutron attenuation coefficients and residual strain maps. The {1 1 0} and {2 1 1} grain families were selected to derive residual strain maps at each angle for strain tomography. Using a small number of angular projections, the filtered back projection (FBP) algorithm was demonstrated for 3D tomographic reconstructions of attenuation and strain. Inspection of internal residual strain in the joint enhanced understanding of residual strain distribution inside the weldment and its effects on crack initiation and mechanical properties.

2. Materials and methods

2.1. Materials and microstructural characterisation

The fabrication and heat treatment procedures of as-received Eurofer97 steels is described in a previous study [24]. Two 6-mm-thick as-received Eurofer97 steel plates with dimension of 150 × 75 × 6 mm^3 were butt-welded to form a laser-welded Eurofer97 joint. The welding processes were made using the single-pass laser welding process via a Yb-fiber laser source with a spot size of 200 μm and a welding speed of 1.2 m/min at The Welding Institute (TWI) to attain a high-quality weld (narrow penetrating bead and slightly concave). For the neutron tomography experiment, a rectangular sample, 56 × 10 × 6 mm^3, was cut from the laser-welded plate of Eurofer97 steel using EDM. The teeth of the comb-shaped sample is usually used to provide reference *d* spacing [25]. In this study, the comb-shaped sample, where the teeth of comb are with dimensions of 4 × 1.5 × 6 mm^3, cut from the same laser-welded plate using EDM. The reference *d* spacings were extracted from different teeth, respectively. The dimensions of the sub-regions of the laser-welded Eurofer97 joint were characterised using reflected light microscopy.

2.2. Angular projections from neutron Bragg edge imaging

The tomographic data was acquired at the IMAT beamline, ISIS neutron spallation source, Rutherford Appleton Laboratory, UK. The weldment was initially placed on a rotating stage in front of the microchannel plate (MCP) detector (Fig. 1**(a)**) with a field view of 28 × 28 mm^2 and pixel resolution of 55 μm (512 × 512 pixels). The field-of-view covers the full fusion zone (FZ), heat-affected zone (HAZ) and part of the base material (BM), where the three different zones are defined by considering the peak temperature, micro-hardness and microstructural changes arising from laser welding and highlighted with red, yellow and grey colours, respectively [26]. Neutron statistics were collected for tomographic reconstruction of attenuation coefficients and lattice spacing. A spatial resolution of 200 μm was achieved by employing an *L*/*D* value of 166 (*L* is the distance from the pinhole collimator to the sample, and *D* is the aperture diameter). As shown in Fig. 1**(b)**, the eight angular projections were obtained by rotating the stage between 0° and 180° in equal angular spacings. At each rotation angle, the data was collected as a stack of wavelength-resolved 2881 radiographs in a range of neutron white beams between 0.7 and 5 Å, which required an exposure time of 2 h for adequate neutron statistics. An open beam data stack was acquired using an exposure time of 30 min without a sample in position.

2.3. Data processing

The attenuation coefficient at each pixel of angular projection ($a(x,y,[03B8])$) was obtained by normalising the transmission data using log transformation. The neutron dose noises were corrected by using the open beam images, which ensured that all the measured projections received the same number of incoming neutrons, considering that the stability of the neutron beam flux is rarely constant for a neutron spallation source [27,28]. The normalisation was performed on the data using a log-transformation. ***Eq. 1***. To complete the tomographic reconstruction, the pixel column of the detector must coincide with the rotation axis of the sample. Due to the difficulties in achieving such concentric rotation, an offset correction is necessary during the data processing (Fig. 1**(c)**). The centred angular attenuation projections were used to construct the sinograms, from which the tomographic slices were reconstructed using the FBP algorithm. The filter of 'Hann', which provides an effective noise reduction, was used for the tomographic reconstruction [29]. The reconstruction process was fulfilled using a built-in mathematical framework of Radon transformation (forward for projection, and inverse for reconstruction) in MATLAB [30]. The 3D tomographic reconstruction ($A(x,y,z)$) was then achieved by combining the tomographic slices (Fig. 1**(d)**). With eight projections and a sample of 10 × 6 mm^2 rectangular cross-section the effective average voxel size is about 2 mm.

$$a(x,y,\theta) = -\log\left(\frac{I(x,y,[03B8])}{I_{op}(x,y,\theta)}\right) \quad (1)$$

where *a* is the attenuation coefficient, *I* and I_{op} are the transmission data and open beam data by summing up the radiograph stack, respectively, x and y indicate the pixel positions in the projections, and θ is the angle at which the projection was scanned.

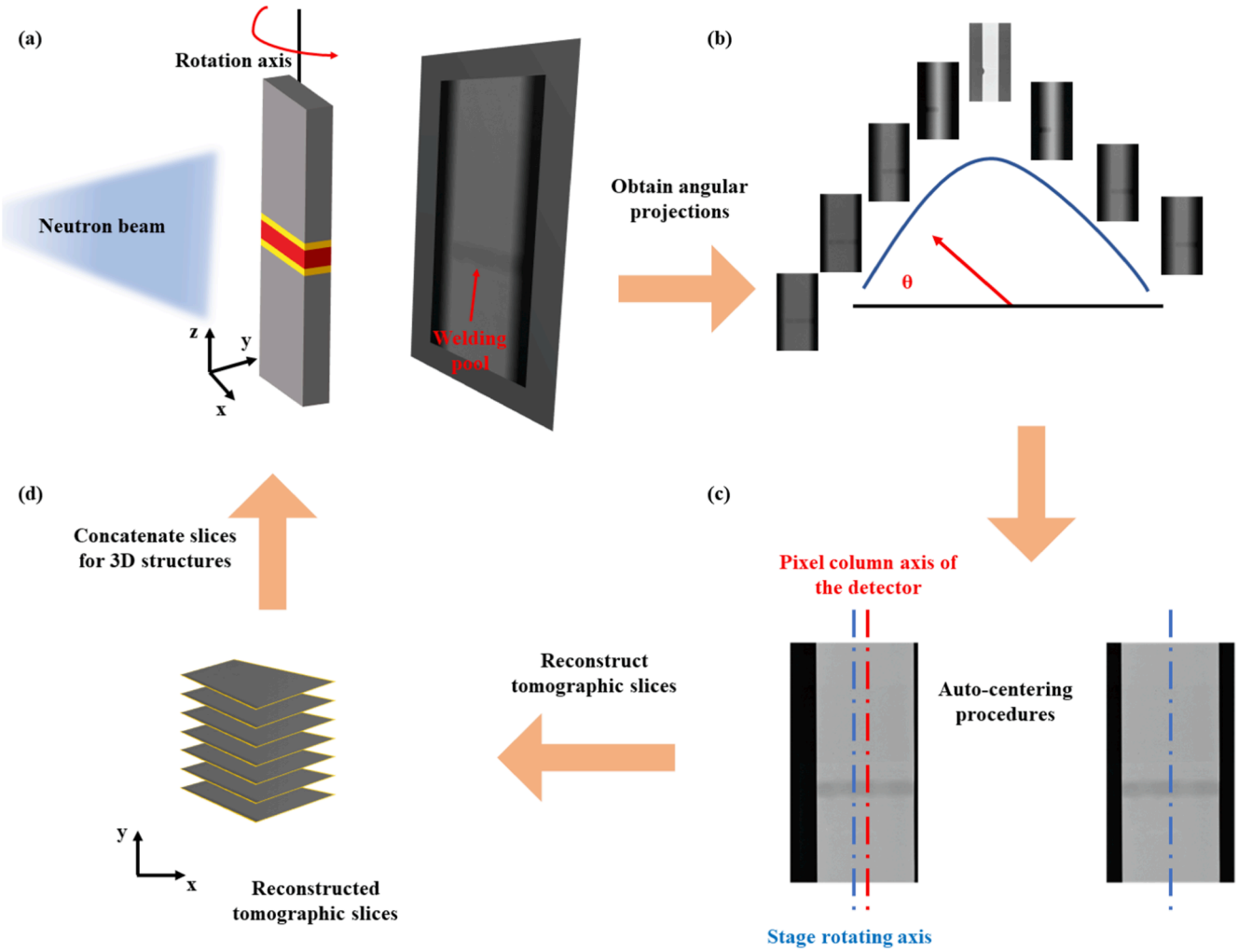

Fig. 1. Schematic figures show the tomographic reconstruction procedures. (a) Experimental setup for NBEI to gain sufficient neutron statistics for attenuation and strain analysis. The axis by which the sample rotates for angular projections is indicated. (b) Angular projections obtained from NBEI during the sample rotation at a constant angular step. (c) Data processing, such as denoising, auto-centring and establishment of sinogram. (d) Reconstruction of tomographic slices by employing the FBP algorithm and the 3D tomographic reconstruction is combined using the tomographic slices.

In general cases, it is crucial to ensure that either compatibility or equilibrium is met to obtain a unique reconstruction, unless some assumptions or constraints are made in some special cases [18,31–33]. Here, to reconstruct the 3D distribution of residual strain, two assumptions are made: (i) The measured strain has minimum sensitivity to the beam directions during the sample rotation. The strain tensor is assumed to be isotropic, and the measured strain has minimal sensitivity to the beam directions during the sample rotation. Given the longitudinal strain typically exhibits greater magnitudes compared to other directions in welded components [34], the assumption permits the tomographic reconstruction of a representative scalar. Whilst it is important to note that this scalar strain based on such an assumption may be best represented by the in-plane hydrostatic component of strain, it still provides valuable insights into the residual strain distribution within the weld. (ii) The effect of texture on determining wavelength positions of Bragg edges at different angular projections is neglected.

The tomographic strain reconstruction was accomplished using the angular residual strain maps ($\varepsilon_{hkl}(x, y, \theta)$) which were derived from angular projections. Fig. 2**(a)** schematically shows that the laser-welded joint is exposed to the neutron beam to acquire the image stacks, each corresponding to a certain wavelength. The Bragg edge transmission spectrum was obtained by dividing the sample image stacks by open-beam image stacks using ImageJ [35], and plotted as a function of wavelength (inset figure in Fig. 2**(a)**). The Bragg edge position was determined by fitting the Bragg edge spectrum via an analytical function [36,37] (***Eq. 2***):

$$T(\lambda) = C_1 + C_2\left[erfc\left(\frac{\lambda_0-\lambda}{\sqrt{2}\sigma}\right) - \exp\left(\frac{\lambda_0-\lambda}{\tau}+\frac{\sigma^2}{2\tau^2}\right)\times erfc\left(\frac{\lambda_0-\lambda}{\sqrt{2}\sigma}+\frac{\sigma}{\sqrt{2}\tau}\right)\right] \quad (2)$$

where λ is the Bragg edge position, σ is the Bragg edge width, τ is the edge asymmetry, C_1 is edge height and C_2 is edge pedestal. The lattice spacing map was determined pixel-by-pixel according to the fitting of the Bragg edge position using ***Eq. 2***. The fitting process was achieved by a C++ fitting tool, TPX_edgefit, using a pixel binning with the macro-pixel size of 5 pixels [38]. The reference lattice spacing was extracted from the teeth of comb-shaped samples in the FZ, HAZ and BM regions. Given the assumption of isotropic strain, reference lattice spacing was obtained from the comb-shaped sample at the scanning angle of 0° and used to calculate residual strain using ***Eq. 3*** for all angular projections. Two grain families, {1 1 0} and {2 1 1}, were selected for residual strain calculation, as the mechanical properties of {2 1 1} grain family are similar to the bulk properties for body centre cubic materials, and the {1 1 0} exhibits the strongest edge contrast.

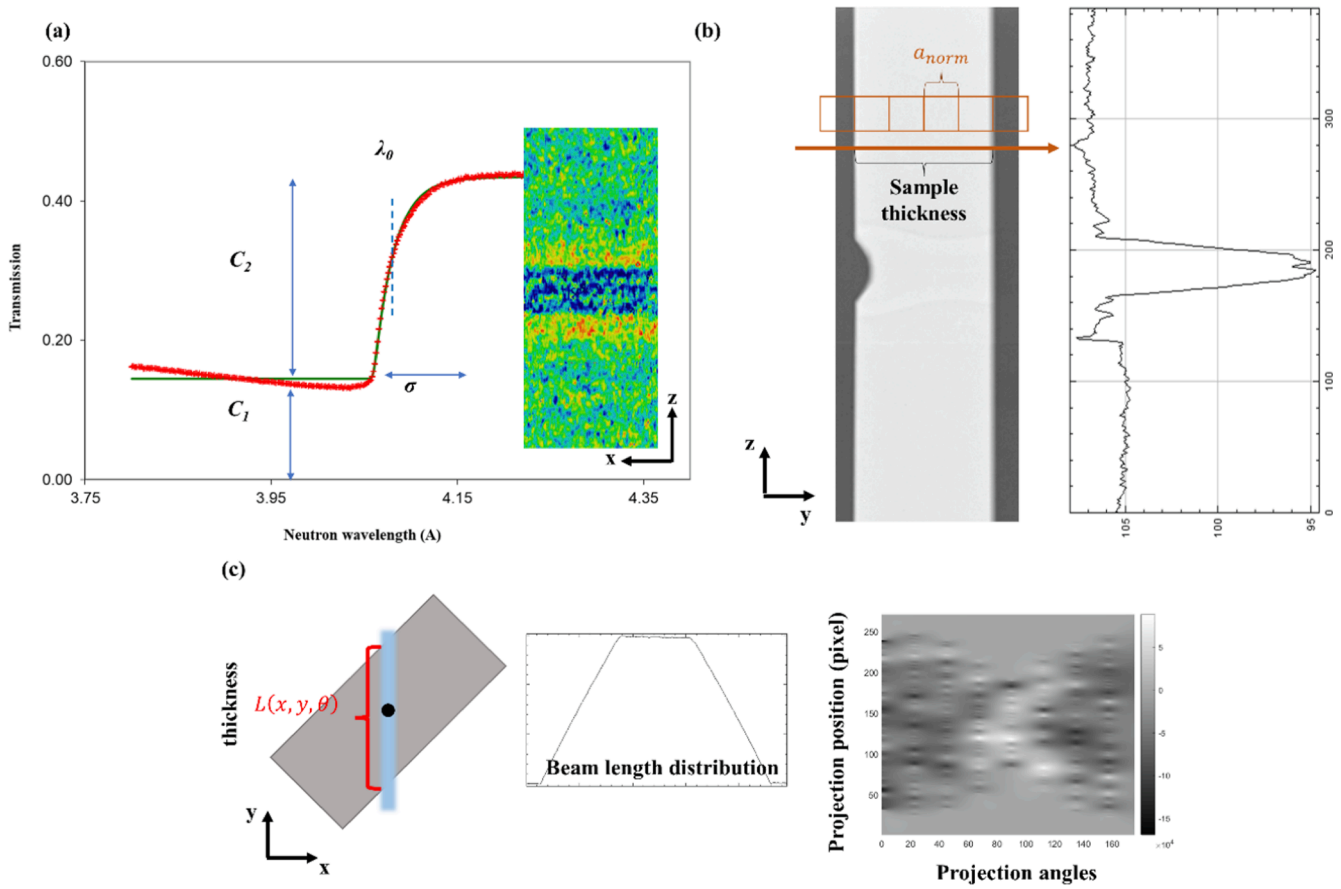

Fig. 2. Data processing for strain tomographic reconstruction. (a) The procedures of Bragg edge fitting and residual strain mapping using the acquired image stacks are presented. (b) The *y*-*z* cross-section of the object showing the beam path length varies along with the joint, and the length is characterised using attenuation coefficients. (c) The *x*-*y* cross-section showing the beam path length which varies with the rotation. The horizontal axis of the box in the middle represents the position of the cross-section, and the vertical axis represents the path length through the sample in the units of pixels. The sinogram of the integral sinogram constructed by multiplying the beam path length is shown on the right.

$$\varepsilon^{hkl} = \frac{\lambda^{hkl} - \lambda_0^{hkl}}{\lambda_0^{hkl}} \tag{3}$$

where λ is the Bragg edge position of the sample, λ_0 is the reference Bragg edge position.

In contrast to the reconstruction of conventional attenuation coefficients, where the angular attenuation projections present the integral neutron absorption over the beam path length using ***Eq. 1***, the angular residual strain maps are the average value over the path. To directly use a well-established reconstruction technique, the experimentally measured average residual strain values must be converted to integral values by multiplying the beam path length ($L(x,y,[03B8])$) using the ***Eq. 4***:

$$\varepsilon_{hkl}^{integral}(x, y, [03B8]) = \varepsilon_{hkl}(x, y, \theta) \bullet L(x, y, \theta) \tag{4}$$

The beam path length was obtained by employing the neutron attenuation coefficient.

The neutron attenuation was obtained from the radiography (Fig. 2 **(b)**). The *y*-*z* cross-section, which showed concave features at the weld region and a uniform distribution at the BM region, was obtained from a scan of the sample around the rotation angle of 90°. The length of the neutron beam path that penetrated the BM region can be derived by measuring the length of sample thickness from the *y*-*z* cross-section. The neutron attenuation coefficients penetrating every pixel (a_{norm}) were normalised by dividing the thickness of the joint at the BM regions. Knowing the normalised attenuation, the length of the neutron beam penetrating the joint can be derived at arbitrary angles from the radiography maps using ***Eq. 5*** (Fig. 2**(c)**). To formulate the strain tomographic reconstruction using widely accepted tomographic reconstruction techniques, an integral strain sinogram was determined by employing the beam path length using ***Eq. 4***. The offset for centring the lattice spacing projection was the same as that of the attenuation reconstruction. The interpolation method of 'v5cubic' was applied at the stage of construction of sinograms using the built-in algorithm in MATLAB to complement the small numbers of projections [30]. Fig. 2**(c)** shows the integral sinogram formed based on residual strain projections.

$$L(x, y, [03B8]) = \frac{a(x, y, [03B8])}{a_{norm}} \tag{5}$$

3. Results

3.1. Attenuation reconstruction

Fig. 3**(a)** shows an oblique view of the 3D attenuation tomographic reconstruction, which determines the shape and dimensions of the FZ and HAZ regions of the Eurofer97 joint. The sub-regions of the joint were distinguishable from the reconstructed model. The fusion line (FZ/HAZ interface) and HAZ/BM interface are indicated using red and yellow dash lines. The reconstructed model matches the shape and dimensions compared to the stitched figure obtained from optical microscopy showing the cross-section of the weldment (Fig. 3**(b)**).

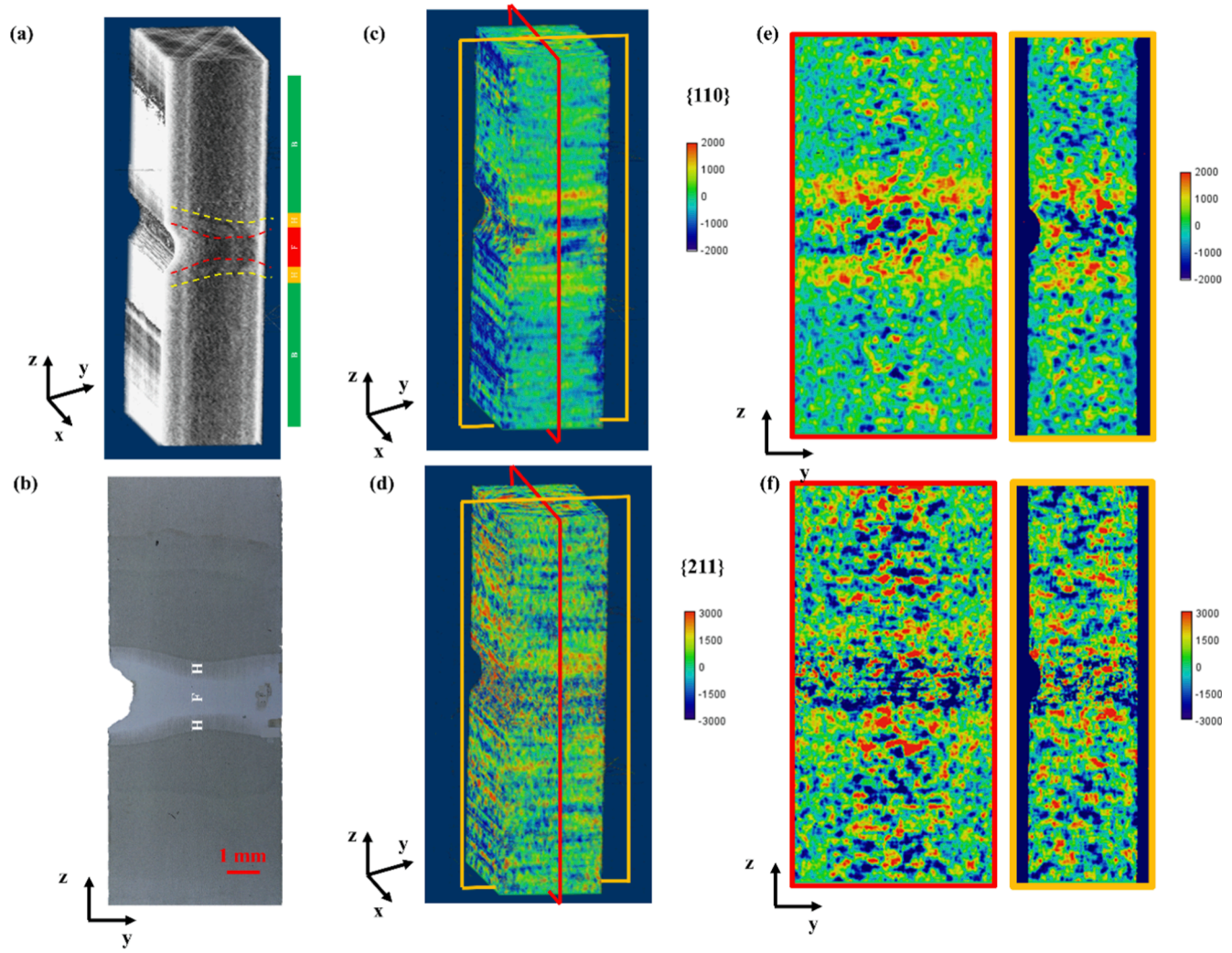

Fig. 3. Results of tomographic reconstruction of laser-welded Eurofer97 joint. (a) The left figure shows the attenuation reconstruction with the concave shape and the structure changes at the welding centre. The red and yellow lines indicate the fusion line and HAZ/BM interface respectively. (b) The cross-section morphology using stitched optical microscopy figures, where the F and H are representative to FZ and HAZ, respectively. (c) and (d) Strain reconstruction using the residual strain maps derived from the {1 1 0} and {2 1 1} grain families, respectively. (e) & (f) Reconstructed tomographic slice derived from the red and orange rectangular slices in (c) and (d), which shows the residual strain distribution in the Euofer97 joint. (For interpretation of the references to colour in this figure legend, the reader is referred to the web version of this article.)

3.2. Residual strain reconstruction

Using the integral residual strain, the tomographic strain reconstruction (Fig. 3**(c)** and Fig. 3**(d)**) was formulated using the {1 1 0} and {2 1 1} grain families, as for the reconstruction of attenuation. The tomographic strain reconstruction of the {1 1 0} grain family shows less noise than that of the {2 1 1} grain family. The residual strain distribution inside the joint was revealed by deriving the residual strain distribution cross-sections. Examples of tomographic slices for the cross-sections at the position highlighted by the red and orange rectangle in Fig. 3**(c)** and Fig. 3**(d)** were obtained. The residual strain distribution of the {1 1 0} and {2 1 1} grain families, for these cross-sections, is presented in Fig. 3**(e)** and Fig. 3**(f)**, where compressive residual strain was found in the FZ, balanced by tensile strain in the HAZ.

3.3. Comparison between experiment-based and post-processed residual strain projections

Post-processing was applied to obtain artificial reconstructed residual strain projections by forward projection of the reconstruction, in order to confirm the precision of the residual strain tomographic reconstruction. Examples are selected at three rotation angles, 0°, 67.5° and 90°, from the 3D reconstruction model, where the residual strain was calculated by averaging strain over the beam path length. Fig. 4 and Fig. 5 illustrate the experiment-obtained and post-processed projections for {1 1 0} and {2 1 1} grain families. The experiment-based residual strain maps at corresponding angles are also presented for comparison.

As shown in Fig. 4**(a)** and Fig. 5**(a)**, the experimental-based projection at 0° reveals the residual compressive strain in the FZ region, balanced by tensile strain in the HAZ region, where a similar residual strain map was reported using NBEI in previous studies on a laser-welded Eurofer97 joint [26]. The residual strain distribution of the {2 1 1} grain family is consistent with the {1 1 0} grain family in terms of trend, with a slight difference in magnitudes at the FZ region. When the sample is rotated, the HAZ region exhibits a more distinct residual tensile strain for the {1 1 0} grain family, and the noise level is decreased. Similarly, the FZ region shows clearest compressive strain in the rotated projections for the {2 1 1} grain family. However, the high strain values are observed around the outer edges of the sample at the projection angle of 67.5° for both grain families, which are likely artifacts of the fitting process. Despite some minor deviations, the post-processed projections (Fig. 4**(b)** and Fig. 5**(b)**) show a similar trend

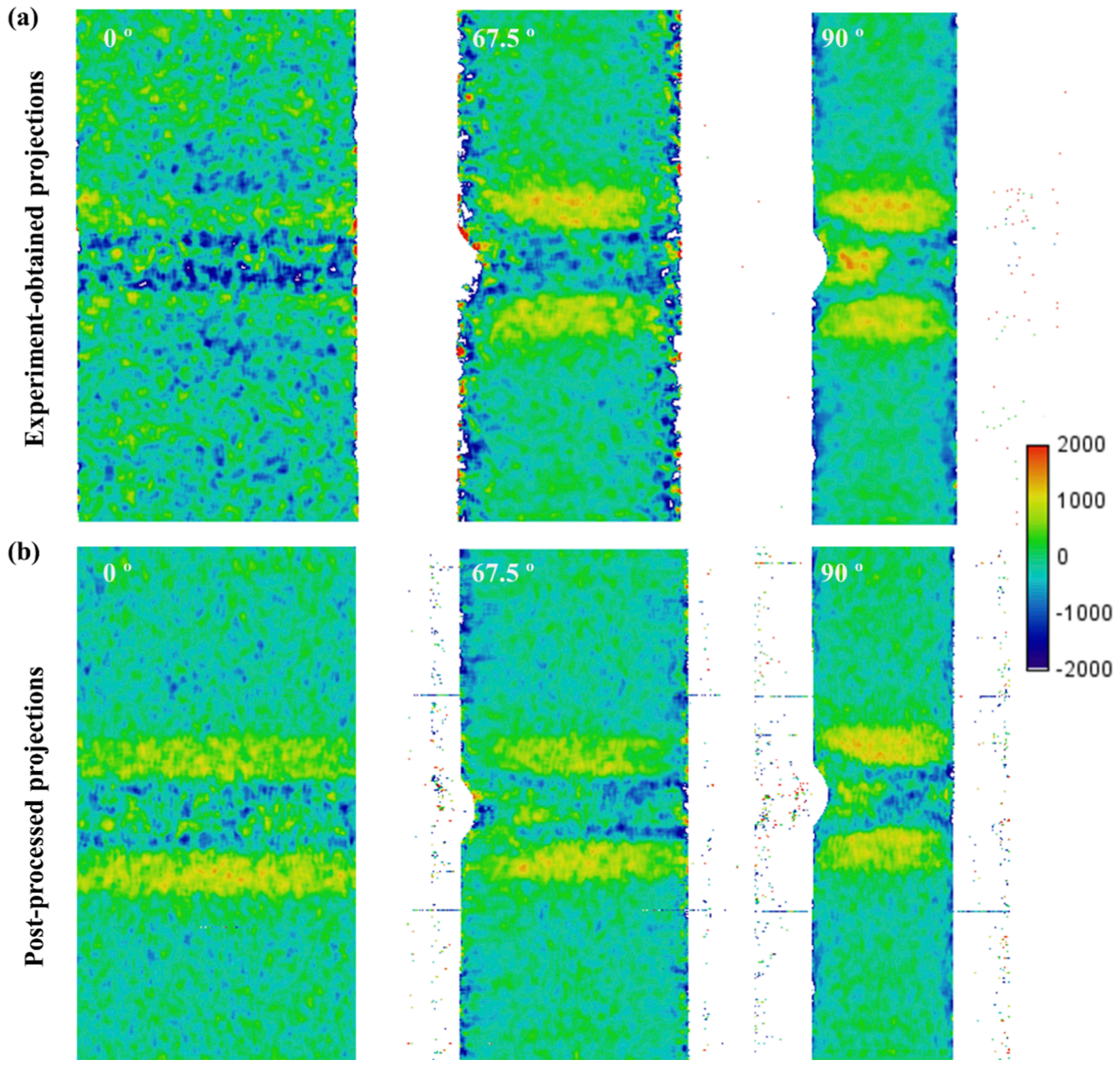

Fig. 4. Residual strain distribution of the {1 1 0} grain family. (a) Experiment-based projections at 0°, 67.5° and 90°. (b) Post-processed projections from tomographic reconstruction averaged over the beam path at the corresponding angles. The colour bar presents the magnitude in micro strain.

and magnitude compared to the experiment-obtained projections for both grain families.

4. Discussion

The experiment-based strain maps of 67.5° and 90° exhibit a better contrast and less noise than the projection of 0° because of larger beam paths with sample rotation, resulting in a ramp-up of collective signal at the same scanning time. The much higher strain values are found in the projection of rotating 67.5°, which is similarly due to the beam path variations, as the thickness of the sample along the neutron beam direction gradually decreases towards the sample edge, leading to noisy Bragg edges for strain analysis. The same phenomenon occurred for both the {1 1 0} and {2 1 1} grain families. By comparing two grain families, see Fig. 3**(c)** and Fig. 3**(d)**, the {1 1 0} grain family exhibits the best contrast and signal-to-noise ratio in the strain maps, which indicates this grain family is the best lattice plane for strain tomographic reconstruction for body central cubic structure [23,39]. However, the magnitude discrepancy of experiment-obtained residual strain maps at the FZ region between two grain families (Fig. 4**(a)** and Fig. 5**(a)**) implies that the {1 1 0} grain family is more susceptible to the intergranular strain [5,26]. To firmly establish the residual strain distribution, it is still necessary to reconstruct the {2 1 1} lattice spacing.

Tomographic reconstruction using a small number of projections is feasible. Fig. 3**(a)** shows prospects of reconstructing the shape and dimension of the sub-region of the weldment with a small number of projections. However, minor defects inside the joint or other microstructural details are of course lacking in such a coarse characterisation due to the compromise in terms of projections, i.e. the counting statistics and the number of projections. The cross-sectional shapes derived from neutron absorption maps was used to determine the normalised attenuation coefficients (a_{norm}) for calculation of beam path length and

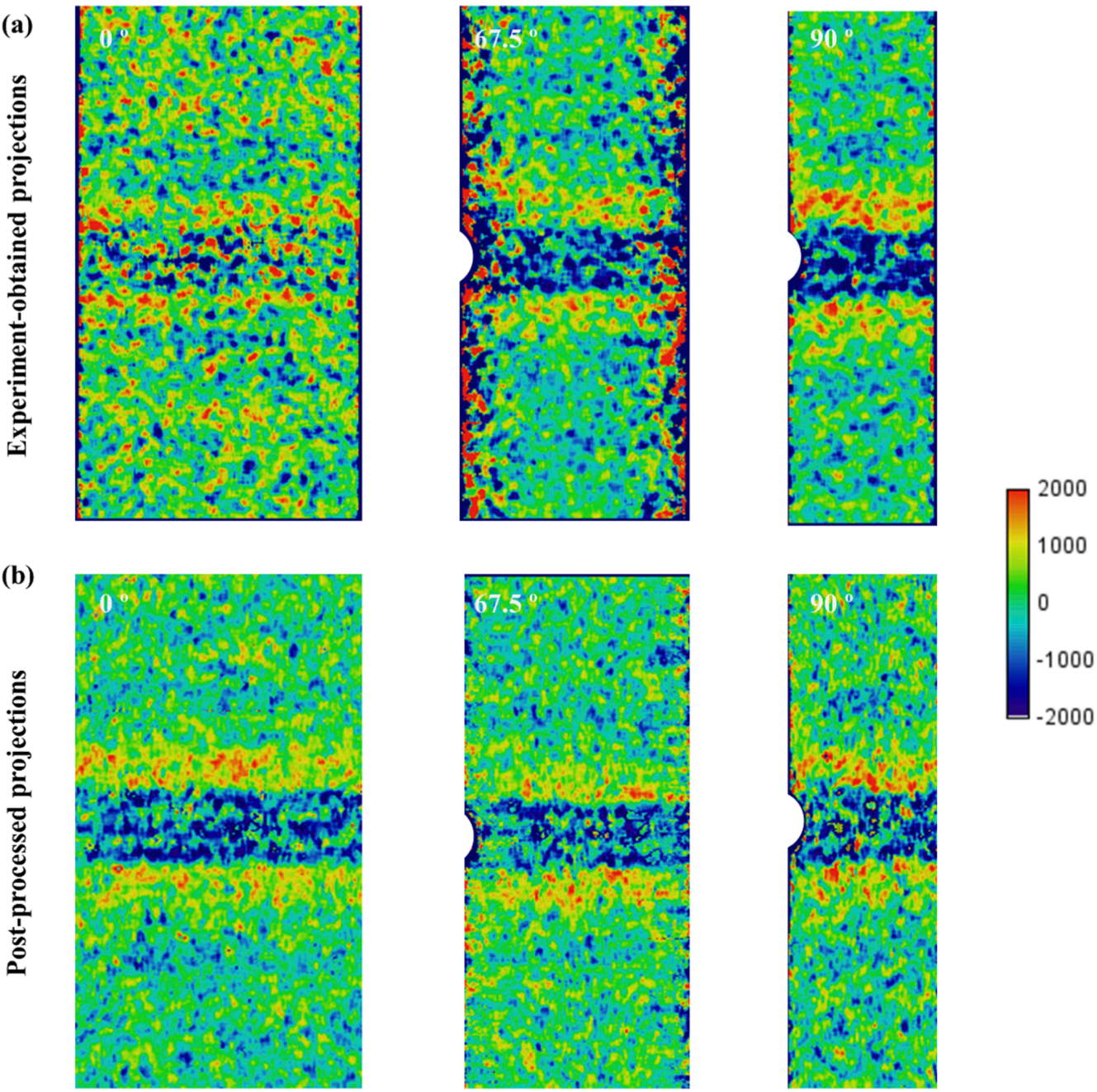

Fig. 5. Residual strain distribution of the {211} grain family. (a) Experiment-based projections at 0°, 67.5° and 90°. (b) Post-processed projections from tomographic reconstruction averaged over the beam path at the corresponding angles. The colour bar presents the magnitude in micro strain.

integral strain calculations (Fig. 2 (b)). In the strain tomographic reconstruction, the resolution of the tomographic slices (Fig. 3**(e)** and Fig. 3**(f)**), derived from red and orange rectangular positions of 3D the reconstruction model, have a higher resolution and less noise because of the higher radial resolution at the centre. Although the interpolation is helpful in enhancing the tomography [40], the radial resolution drops for a location far from the rotation centre compared to those reconstructed from large numbers of projections [14,27]. Comparison between tomographic slices and experiment-based tomographic projections implies that the residual strain is uniformally distributed in the joint. Furthermore, the consistency between experimental-based and post-processed tomographic projections (Fig. 4**(a)** and Fig. 5**(a)**), at three selective angles, indicates that the direct use of the FBP algorithm can be applied to strain reconstruction for a small number of projections and provides a valuable justification for the assumptions made in this study. However, the slight divergence observed at 0°, which is thought to result from an issue regarding the uniqueness of the reconstruction where a given boundary deformation does not uniquely define the strain field within an object [13]. While the forward calculation can provide valuable insight into the validity of the reconstruction, an infinite number of strain fields can give rise to the same measurement profile, which can introduce uncertainty in the post-processing strain map. Moreover, the application of interpolation techniques to decrease the level of noise in the tomographic reconstruction may also introduce artefacts that can further complicate the analysis. Our future work will involve the collection of more data through optimised neutron flux and projections to improve the resolution and accuracy of the strain map and tomographic reconstruction. Due to the insufficient neutron flux at current neutron sources the necessary acquisition time is too long for strain evaluation, as acquiring a large stack of strain maps is challenging

to realise [23,40,41]. To solve this issue, a deep learning or FE method may provide new opportunities to predict or simulate strain projections to reduce the data acquisition time [13,16,28,42].

As opposed to neutron or synchrotron diffraction, which yield spatially resolved strain maps at the expense of longer acquisition time, neutron imaging offers unique capability for tomographic reconstruction because of the capacity of deriving projections for a large region [10,19,41,43]. Such capability also makes it applicable for investigating complex structures manufactured from exotic materials unsuitable for conventional non-destructive evaluation methods. The detailed residual strain distribution derived from the tomographic reconstruction can be deemed a precursor for understanding crack initiation and propagation. The internal residual strain field also provides insight into designing and optimising the manufacturing process for structural integrity and extending longevity.

Owing to the transmission geometry, the two main features of strain measurements using NBEI are that the strain magnitude is averaged through the sample thickness and that the probed strain direction is always along the incident beam direction. Because of the tensorial properties of strain, a precise determination using tomography is not straightforward. It was shown that reconstruction of strain is not possible in the general sense. However, for specific cases, when certain assumptions and/or boundary conditions, such as symmetry weighting of strain components, can be made, the tomographic reconstruction of strain components is possible [13–18]. Here, the residual strain in the Euofer97 joint is deemed an isotropic state as previous studies presented a similar residual strain distribution in three principal directions. To directly reconstruct strain without any assumptions, further efforts are still necessary to solve the directional issue of strain measured by NBEI. Consideration of the specific design of transmission geometry by positioning detector at an angle to constantly measure the strain along the rotating axial direction or decomposition of strain by employing finite element analysis might help overcome current limitations.

5. Conclusion

Attenuation and strain tomographic reconstruction has been accomplished by angular projections derived from NBEI using the FBP algorithm. The principal conclusions of this study are:

1. The attenuation tomograph exhibits a concave shape and dimensions matching those of the sub-regions of the joint, in good agreement with the stitched reflected light micrographs image.
2. The reconstructed tomographic slices present a similar strain distribution to the conventional neutron diffraction and Bragg edge imaging residual strain measurements, implying a uniform strain distribution in the joint.
3. The post-processed projections, at three selected angles, agree with the experiment-based projections.

These findings demonstrate the feasibility of the direct use of the FBP algorithm in strain tomographic reconstruction with a small number of projections, and with the internal residual strain distribution providing insight into understanding the connections between residual strain and crack initiation in engineering components.

CRediT authorship contribution statement

Bin Zhu: Methodology, Investigation, Formal analysis, Writing – original draft, Writing – review & editing. **Nathanael Leung:** Investigation, Writing – review & editing. **Winfried Kockelmann:** Investigation, Writing – review & editing. **Michael Gorley:** Supervision, Writing – review & editing. **Mark J. Whiting:** Supervision, Writing – review & editing. **Yiqiang Wang:** Supervision, Conceptualization, Methodology, Writing – review & editing. **Tan Sui:** Supervision, Conceptualization, Methodology, Writing – review & editing.

Declaration of Competing Interest

The authors declare that they have no known competing financial interests or personal relationships that could have appeared to influence the work reported in this paper.

Data availability

Data will be made available on request.

Acknowledgements

The authors give thanks to the Karlsruhe Institute of Technology for providing the Eurofer97 plate for this study and Dr Simon Kirk (UKAEA) for his advice on laser welding. The authors thank the ISIS neutron and muon source for providing the beamtime at IMAT (DOI:10.5286/ISIS.E.RB1920513) facilities. This work has been carried out within the framework of the EUROfusion Consortium, funded (part) by the European Union via the Euratom Research and Training Programme (Grant Agreement No 101052200 — EUROfusion). Views and opinions expressed are however those of the author(s) only and do not necessarily reflect those of the European Union or the European Commission. Neither the European Union nor the European Commission can be held responsible for them. Dr Wang and Dr Gorley would also like to acknowledge the EPSRC grant (EP/W006839/1) and the Department for Energy Security and Net Zerofor their time and resources. Dr Sui would like to acknowledge funding from the Royal Academy of Engineering under the Industrial Fellowships programme.

References

[1] P. Fernández, A.M. Lancha, J. Lapeña, M. Serrano, M. Hernández-Mayoral, Metallurgical properties of reduced activation martensitic steel Eurofer'97 in the as-received condition and after thermal ageing, J. Nucl. Mater. 307–311 (2002) 495–499, https://doi.org/10.1016/S0022-3115(02)01013-9.
[2] X. Li, X. Li, S. Schönecker, R. Li, J. Zhao, L. Vitos, Understanding the mechanical properties of reduced activation steels, Mater Des. 146 (2018) 260–272, https://doi.org/10.1016/j.matdes.2018.03.009.
[3] R. Lässer, N. Baluc, J.L. Boutard, E. Diegele, S. Dudarev, M. Gasparotto, A. Möslang, R. Pippan, B. Riccardi, B. van der Schaaf, Structural materials for DEMO: the EU development, strategy, testing and modelling, Fusion Eng. Des. 82 (2007) 511–520, https://doi.org/10.1016/j.fusengdes.2007.06.031.
[4] R. Andreani, E. Diegele, R. Laesser, B. Van Der Schaaf, The european integrated materials and technology programme in fusion, in, J. Nucl. Mater. North-Holland (2004) 20–30, https://doi.org/10.1016/j.jnucmat.2004.04.339.
[5] B. Zhu, Y. Wang, J. Dluhoš, A.J. London, M. Gorley, M.J. Whiting, T. Sui, A novel pathway for multiscale high-resolution time-resolved residual stress evaluation of laser-welded Eurofer97, Sci. Adv. 8 (2022), https://doi.org/10.1126/sciadv.abl4592.
[6] S. Kirk, W. Suder, K. Keogh, T. Tremethick, A. Loving, Laser welding of fusion relevant steels for the European DEMO, Fusion Eng. Des. (2018), https://doi.org/10.1016/j.fusengdes.2018.03.039.
[7] H. Tanigawa, T. Maruyama, Y. Noguchi, N. Takeda, S. Kakudate, Laser welding to expand the allowable gap in bore welding for ITER blanket hydraulic connection, Fusion Eng. Des. 98–99 (2015) 1634–1637, https://doi.org/10.1016/j.fusengdes.2015.06.155.
[8] Y. Wang, R. Kannan, L. Li, Insight into type IV cracking in Grade 91 steel weldments, Mater Des. 190 (2020), 108570, https://doi.org/10.1016/j.matdes.2020.108570.
[9] P.J. Withers, Residual stress and its role in failure, Rep. Prog. Phys. 70 (2007) 2211–2264, https://doi.org/10.1088/0034-4885/70/12/R04.
[10] C. Yildirim, C. Jessop, J. Ahlström, C. Detlefs, Y. Zhang, 3D mapping of orientation variation and local residual stress within individual grains of pearlitic steel using synchrotron dark field X-ray microscopy, Scr Mater. 197 (2021), 113783, https://doi.org/10.1016/j.scriptamat.2021.113783.
[11] G.S. Schajer, Practical Residual Stress Measurement Methods (2013), https://doi.org/10.1002/9781118402832.
[12] W. Chen, T. Voisin, Y. Zhang, J.-B. Florien, C.M. Spadaccini, D.L. McDowell, T. Zhu, Y.M. Wang, Microscale residual stresses in additively manufactured stainless steel, Nat. Commun. 10 (2019), https://doi.org/10.1038/s41467-019-12265-8.
[13] W.R.B. Lionheart, P.J. Withers, Diffraction tomography of strain, Inverse Probl. 31 (2015), 045005, https://doi.org/10.1088/0266-5611/31/4/045005.
[14] R. Woracek, J. Santisteban, A. Fedrigo, M. Strobl, Diffraction in neutron imaging—a review, Nucl. Instrum. Methods Phys. Res. A. 878 (2018) 141–158, https://doi.org/10.1016/j.nima.2017.07.040.

[15] B. Abbey, S.Y. Zhang, W.J.J. Vorster, A.M. Korsunsky, Feasibility study of neutron strain tomography, in: Procedia Eng, Elsevier Ltd, 2009: pp. 185–188. https://doi.org/10.1016/j.proeng.2009.06.043.
[16] B. Abbey, S.Y. Zhang, W. Vorster, A.M. Korsunsky, Reconstruction of axisymmetric strain distributions via neutron strain tomography, Nucl. Instrum. Methods Phys. Res. B. 270 (2012), https://doi.org/10.1016/j.nimb.2011.09.012.
[17] B. Abbey, S.Y. Zhang, M. Xie, X. Song, A.M. Korsunsky, Neutron strain tomography using Bragg-edge transmission, Int. J. Mater. Res. 103 (2012) 234–241, https://doi.org/10.3139/146.110674.
[18] C.M. Wensrich, J.N. Hendriks, A. Gregg, M.H. Meylan, V. Luzin, A.S. Tremsin, Bragg-edge neutron transmission strain tomography for in situ loadings, Nucl. Instrum. Methods Phys. Res. B. 383 (2016) 52–58, https://doi.org/10.1016/j.nimb.2016.06.012.
[19] A.M. Korsunsky, N. Baimpas, X. Song, J. Belnoue, F. Hofmann, B. Abbey, M. Xie, J. Andrieux, T. Buslaps, T.K. Neo, Strain tomography of polycrystalline zirconia dental prostheses by synchrotron X-ray diffraction, Acta. Mater. 59 (2011) 2501–2513, https://doi.org/10.1016/j.actamat.2010.12.054.
[20] N. Kardjilov, I. Manke, R. Woracek, A. Hilger, J. Banhart, Advances in neutron imaging, Mater. Today 21 (2018) 652–672, https://doi.org/10.1016/j.mattod.2018.03.001.
[21] R. Woracek, D. Penumadu, N. Kardjilov, A. Hilger, M. Boin, J. Banhart, I. Manke, 3D mapping of crystallographic phase distribution using energy-selective neutron tomography, Adv. Mater. 26 (2014) 4069–4073, https://doi.org/10.1002/adma.201400192.
[22] A. Reid, M. Marshall, S. Kabra, T. Minniti, W. Kockelmann, T. Connolley, A. James, T.J. Marrow, M. Mostafavi, Application of neutron imaging to detect and quantify fatigue cracking, Int. J. Mech. Sci. 159 (2019) 182–194, https://doi.org/10.1016/j.ijmecsci.2019.05.037.
[23] M. Busi, E. Polatidis, F. Malamud, W. Kockelmann, M. Morgano, A. Kaestner, A. Tremsin, N. Kalentics, R. Logé, C. Leinenbach, T. Shinohara, M. Strobl, Bragg edge tomography characterization of additively manufactured 316L steel, Phys. Rev. Mater. 6 (2022), 053602, https://doi.org/10.1103/PhysRevMaterials.6.053602.
[24] M. Rieth, M. Schirra, A. Falkenstein, P. Graf, S. Heger, H. Kempe, R. Lindau, H. Zimmermann, EUROFER 97 Tensile, charpy, creep and structural tests, Germany, 2003. http://inis.iaea.org/search/search.aspx?orig_q=RN:35032617.
[25] P.J. Withers, M. Preuss, A. Steuwer, J.W.L. Pang, Methods for obtaining the strain-free lattice parameter when using diffraction to determine residual stress, J. Appl. Crystallogr. 40 (2007) 891–904, https://doi.org/10.1107/S0021889807030269.
[26] B. Zhu, N. Leung, W. Kockelmann, S. Kabra, A.J. London, M. Gorley, M.J. Whiting, Y. Wang, T. Sui, Revealing the residual stress distribution in laser welded Eurofer97 steel by neutron diffraction and Bragg edge imaging, J. Mater. Sci. Technol. 114 (2022) 249–260, https://doi.org/10.1016/j.jmst.2021.12.004.
[27] T. Minniti, F. Schoofs, L.M. Evans, W. Kockelmann, J.H. You, H. Lewtas, Structural integrity of DEMO divertor target assessed by neutron tomography, Fusion Eng. Des. 169 (2021), https://doi.org/10.1016/j.fusengdes.2021.112661.
[28] D. Micieli, T. Minniti, L.M. Evans, G. Gorini, Accelerating Neutron Tomography experiments through Artificial Neural Network based reconstruction, Sci. Rep. 9 (2019), https://doi.org/10.1038/s41598-019-38903-1.
[29] M. Lyra, A. Ploussi, Filtering in SPECT image reconstruction, Int. J. Biomed. Imaging. (2011), https://doi.org/10.1155/2011/693795.
[30] A.C. Kak, M. Slaney, G. Wang, Principles of computerized tomographic imaging, Med. Phys. 29 (2002), https://doi.org/10.1118/1.1455742.
[31] J.N. Hendriks, A.W.T. Gregg, R.R. Jackson, C.M. Wensrich, A. Wills, A.S. Tremsin, T. Shinohara, V. Luzin, O. Kirstein, Tomographic Reconstruction of Triaxial Strain Fields from Bragg-Edge Neutron Imaging, 2019. https://arxiv.org/pdf/1906.08506.pdf (accessed October 3, 2019).
[32] A.W.T. Gregg, J.N. Hendriks, C.M. Wensrich, A. Wills, A.S. Tremsin, V. Luzin, T. Shinohara, O. Kirstein, M.H. Meylan, E.H. Kisi, Tomographic reconstruction of two-dimensional residual strain fields from bragg-edge neutron imaging, Phys. Rev. Appl. 10 (2018), https://doi.org/10.1103/PhysRevApplied.10.064034.
[33] J.N. Hendriks, A.W.T. Gregg, C.M. Wensrich, A.S. Tremsin, T. Shinohara, M. Meylan, E.H. Kisi, V. Luzin, O. Kirsten, Bragg-edge elastic strain tomography for in situ systems from energy-resolved neutron transmission imaging, Phys. Rev. Mater. 1 (2017), https://doi.org/10.1103/PhysRevMaterials.1.053802.
[34] T. Nitschke-Pagel, Recommendations for the measurement of residual stresses in welded joints by means of X-ray diffraction—results of the WG6-RR test, Welding in the World 65 (2021), https://doi.org/10.1007/s40194-020-01029-4.
[35] C.A. Schneider, W.S. Rasband, K.W. Eliceiri, NIH Image to ImageJ: 25 years of image analysis, Nat. Methods. 9 (2012) 671–675, https://doi.org/10.1038/nmeth.2089.
[36] J.R. Santisteban, L. Edwards, A. Steuwer, P.J. Withers, Time-of-flight neutron transmission diffraction, J. Appl. Crystallogr. 34 (2001) 289–297, https://doi.org/10.1107/S0021889801003260.
[37] A. Steuwer, P.J. Withers, J.R. Santisteban, L. Edwards, G. Bruno, M.E. Fitzpatrick, M.R. Daymond, M.W. Johnson, D. Wang, Bragg edge determination for accurate lattice parameter and elastic strain measurement, Physica. Status Solidi A Appl. Res. 185 (2001) 221–230, https://doi.org/10.1002/1521-396X(200106)185:2<221::AID-PSSA221>3.0.CO;2-C.
[38] A.S. Tremsin, T.Y. Yau, W. Kockelmann, Non-destructive examination of loads in regular and self-locking spiralock® threads through energy-resolved neutron imaging, Strain 52 (2016) 548–558, https://doi.org/10.1111/str.12201.
[39] B. Zhu, N. Leung, Y. Wang, H. Zhang, J. Dluhoš, T. Pirling, M. Gorley, M. J. Whiting, T. Sui, Investigation of the residual strain and deformation mechanisms in laser-welded Eurofer97 steel for fusion reactors, Mater. Sci. Eng. A 877 (2023), 145147, https://doi.org/10.1016/j.msea.2023.145147.
[40] H.G. Kim, H. Yoo, Image enhancement for computed tomography using directional interpolation for sparsely-sampled sinogram, Optik. (Stuttg). 166 (2018), https://doi.org/10.1016/j.ijleo.2018.03.139.
[41] H.J. Kirkwood, S.Y. Zhang, A.S. Tremsin, A.M. Korsunsky, N. Baimpas, B. Abbey, Neutron strain tomography using the radon transform, Mate.r Today Proc. (2015), https://doi.org/10.1016/j.matpr.2015.05.057.
[42] X. Yang, V. de Andrade, W. Scullin, E.L. Dyer, N. Kasthuri, F. de Carlo, D. Gürsoy, Low-dose x-ray tomography through a deep convolutional neural network, Sci. Rep. 8 (2018), https://doi.org/10.1038/s41598-018-19426-7.
[43] A.W.T. Gregg, J.N. Hendriks, C.M. Wensrich, V. Luzin, A. Wills, Neutron diffraction strain tomography: demonstration and proof-of-concept, Rev. Sci. Instrum. 91 (2020), https://doi.org/10.1063/1.5120422.